

# MASSIVE QUIESCENT CORES IN ORION. IV. THEIR SUPERCRITICAL STATE REVEALED BY HIGH RESOLUTION AMMONIA MAPS

D. LI<sup>1,2,3</sup>, J. KAUFFMANN<sup>3</sup>, Q. ZHANG<sup>4</sup>, W. CHEN<sup>5</sup>

*Draft version July 6, 2012*

## ABSTRACT

We present combined VLA and GBT images of NH<sub>3</sub> inversion transitions (1,1) and (2,2) toward OMC2 and OMC3. We focus on the relatively quiescent Orion cores, which are away from the Trapezium cluster and have no sign of massive protostars nor evolved star formation, such as IRAS source, water maser, and methanol maser. The 5'' angular resolution and 0.6 km s<sup>-1</sup> velocity resolution of these data enable us to study the thermal and dynamic state of these cores at  $\sim 0.02$  pc scales, comparable to or smaller than those of the current dust continuum surveys. We measure temperatures for a total of 30 cores, with average masses and radii of 11 M<sub>⊙</sub> and 0.039 pc, respectively. Compared to other Gould Belt dense cores, the Orion cores have an unusually high gravitational-to-kinetic energy ratio (virial mass ratio  $R_{vir} \gg 1$ ), resembling results for other clouds forming high-mass stars. This results from Orion cores having velocity dispersions similar to those in, e.g., Perseus and Ophiuchus, but higher masses for given sizes. 12 out of 30 cores are associated with embedded YSOs, which are identified by Spitzer. These Protellar cores have a mean mass of 16.5 M<sub>⊙</sub> versus 7.3 M<sub>⊙</sub> for that of the starless cores. 14 of starless massive Orion cores are supercritical (mass-to-critical-mass ratio  $R_c > 1$ ). These massive Orion starless cores will likely collapse or fragment relatively quickly and can thus be considered direct precursors to protostars.

*Subject headings:* ISM:clouds – individual (Orion) – Stars:formation – instrumentation: interferometers

## 1. INTRODUCTION

Stars form in molecular clouds. Within molecular clouds, discrete structures with observable column density contrast, particularly in high density tracers, with its surroundings are referred to as cores (e.g. Benson & Myers 1989; Ward-Thompson et al. 2007). The relatively high extinction and density of cores make them the likely site for the onset of collapse, which could lead to star formation.

Recent core surveys (e.g. Ikeda et al. 2007; Könyves et al. 2010; Sadavoy et al. 2010) are facilitated by focal plane imaging arrays of growing sizes. Although many surveys have large sample size in the hundreds, the majority of these studies are of dust continuum with one of the major focus being the core mass function. Direct measurement of cores' thermal and dynamic structures require spectra maps of high density tracers and preferably cover the same spatial dynamic ranges as those of the dust emission.

There is a clear dichotomy between low mass star formation and high mass star formation. Massive stars are formed exclusively in giant molecular clouds and with higher efficiency. Due to the large distances of most massive star forming regions, many massive cores are under-resolved, showing signs of star formation well underway, such as H<sub>2</sub>O masers (Mookerjee et al. 2004)

and/or compact HII regions (Reid & Wilson 2005). At about 437 pc (Hirota et al. 2007; Menten et al. 2007), Orion molecular clouds are the closest massive star forming region with an OB cluster, thus particularly suited for studying the early stages of star formation in massive cores and/or under the influence of young massive stars. In a series of papers, we identified quiescent clouds/cores (containing no HII region, no IRAS point sources, and are at least 1 pc away from the OB cluster) in Orion with NH<sub>3</sub> and N<sub>2</sub>H<sup>+</sup> with a beam size of about 1' (Li, Goldsmith & Menten 2003; hereafter paper I), presented high resolution 350  $\mu$ m images with a beam size of 9'' (Li et al. 2007; hereafter paper II), and revealed that two thirds of Orion cores have signatures of ongoing dynamic evolution, both outflows and inflows (Velusamy et al. 2008 hereafter paper III). Based on dust mass and dust core size (paper II), the majority of the cores are seemingly supercritical, i.e., no adequate support from thermal pressure, turbulence, or static magnetic field. This is consistent with the majority of the cores being hydrostatically unstable (paper III), which, however, could not be directly tested due to a lack of high resolution spectroscopic data.

Spectroscopic survey of CO 1-0 (Williams, Plambeck & Heyer 2003) and CO 3-2 (Takahashi et al. 2008) reveal that part of the Orion molecular cloud, namely, OMC2 and OMC3, contains many molecular outflows. OMC2 and OMC3 have also been mapped in high density tracers. Using the Nobeyama 45m telescope, Tatematsu et al. (2008) identified 34 cloud cores in N<sub>2</sub>H<sup>+</sup> 1-0 with a beam width of around 18''. Ikeda et al. (2007) studied dense gas in the same region using H<sup>13</sup>CO<sup>+</sup> also with Nobeyama. These studies find higher column density for respective tracers compared with low mass star forming

<sup>1</sup> National Astronomical Observatories, Chinese Academy of Science, Chaoyang District Datun Rd A20, Beijing, China; email: ithaca.li@gmail.com

<sup>2</sup> Space Science Institute, Boulder, CO

<sup>3</sup> Jet Propulsion Laboratory, California Institute of Technology, Pasadena, CA, USA

<sup>4</sup> Harvard-Smithsonian Center for Astrophysics, Cambridge, MA, USA

<sup>5</sup> Peking University, Beijing, China

regions, such as Taurus.  $\text{NH}_3$  inversion transitions are particularly suited for studying dense cores due to their lack of depletion and their sensitivity to kinetic temperature (Ho & Townes 1983). Wiseman & Ho (1998) obtained  $\text{NH}_3$  maps of a  $8' \times 6'$  region around Orion-KL using VLA. The gas morphology there is dominated by quasi-parallel filaments severely influenced by the energy output of young massive stars.

In this letter, we present the combined VLA and GBT ammonia survey of the cores in OMC2 and OMC3. The spatial resolution of  $\sim 5''$  and the spectral resolution of  $0.6 \text{ km/s}$  facilitate a detailed examination of the thermal and dynamic states of massive 'quiescent' Orion cores.

## 2. OBSERVATIONS AND DATA REDUCTION

The VLA observations of OMC2/OMC3 were carried out in the D configuration on July 29 and September 24 of 2000. We used the correlator mode 4 to cover the  $\text{NH}_3$  (J,K) = (1,1) and (2,2) inversion transitions simultaneously. With a primary beam of about  $2'$  at the observing frequencies, a total of 20 pointings were used to mosaic the OMC2/3 regions. The correlator was configured to a bandwidth of 3.13 MHz for each transition that was divided into 64 channels, providing a velocity coverage of  $40 \text{ km/s}$  in  $0.6 \text{ km/s}^{-1}$  channel spacing. In both observations, we used quasar 3C286 as the flux calibrator, 3C84 or 3C273 as bandpass calibrators, respectively. The time dependent gains were monitored by observing 0539-057 or 0605-085. Visibility data were calibrated in AIPS and exported to MIRIAD for further imaging. The  $1\sigma$  RMS in the channel maps, after combining the two observations is about 8 mJy per spectral channel.

The observations of  $\text{NH}_3$  (1,1) and (2,2) transitions with the GBT were taken on April 6th and 7th of 2005 in the OTF mode using the receiver Rcvr18-26. The correlator setup had a 200 MHz bandwidth and  $0.31 \text{ km/s}^{-1}$  velocity resolution (8192 channels). The flat baseline and the wide bandwidth allowed us to use frequency switch with a throw of 12.5 MHz. The spectra were folded and the 3D data cube were resampled to a grid of  $12''$  spacing and  $0.3 \text{ km/s}^{-1}$  channel. The resulting GBT spectra has a typical 0.12 K RMS noise per channel.

We combine the  $\text{NH}_3$  data from the VLA with those from the GBT to recover missing short spacing fluxes in the interferometric data. The combination was performed in the UV domain using MIRIAD, following the procedure outlined in Vogel et al. (1984) and Zhang et al. (2000). The  $\text{NH}_3$  emission from the combined image, when convolved to the  $30''$  GBT beam, recovers more than 80% of the fluxes detected in the GBT data. The integrated intensity of the  $\text{NH}_3$  (1,1) line with previously identified continuum sources and a pair of typical spectra are presented in Fig. 1.

## 3. DERIVATION OF KINETIC TEMPERATURE AND VELOCITY DISPERSION

Largely following Ho & Townes (1983), Paper I described a recipe for deriving kinetic temperature from spectrally resolved, modestly blended  $\text{NH}_3$  lines (intrinsic line width  $\Delta V \sim 1.0 \text{ km/s}$ ). In this paper, we report line width  $\Delta V$  in FWHM. The one dimensional velocity dispersion  $\sigma$  used in Eq. 8, Eq. 11 and Eq. 12 is related to FWHM as  $\Delta V = \sqrt{8 \ln(2)} \sigma$  for a Gaussian. The key step is to obtain the optical depth of the

(1,1) line from simultaneously fitting all hyperfine components. As can be seen in Fig. 1, the VLA band is not wide enough to fully cover the two outer groups (*osg*). The combined data set thus only have the main and inner satellite components of the (1,1) transition and have a velocity resolution of  $0.6 \text{ km/s}$ . Toward most positions, the intrinsic line width is smaller or approaching channel width. For such under-resolved line, the opacity cannot be easily uniquely fitted.

We developed a more straightforward recipe utilizing two ratios between integrated intensities, which are directly observable,  $\mathcal{R}^{12} = [\int T_A^{(mg+isg)}(1,1) d\nu] / [\int T_A(2,2) d\nu]$  and  $\mathcal{R}^{sm} = [\int T_A^{(isg)}(1,1) d\nu] / [\int T_A^{(mg)}(1,1) d\nu]$ . The rotational temperature can be derived as the following

$$T_R = 41.5 \text{ K} / \ln [1.06 \times \mathcal{C}(1,1) \times R^{12}] , \quad (1)$$

where  $\mathcal{C}(1,1)$  is a correction factor numerically determined as

$$\mathcal{C}(1,1) = 0.003 + 2.26 \mathcal{R}^{sm} + 0.00032 e^{5.38 \mathcal{R}^{sm}} , \quad (2)$$

which is based on fitting to simulated  $\text{NH}_3$  (1,1) spectra generated with a grid of opacities and linewidth. The kinetic temperature is then (paper I)

$$T_k = 3.67 + 0.307 \times T_R + 0.0357 \times T_R^2 . \quad (3)$$

The full recipe is given in Kauffmann et al. (2012) and is generally applicable to a wide range of conditions in opacities, channel width, and intrinsic linewidth. The uncertainty in derived kinetic temperature is then calculated using a Monte Carlo approach (paper I). For pixels with (2,2) detection, the representative  $1\sigma$  uncertainty is about 1 to 2 K for emission peaks and between 2 K and 5 K for diffuse areas. Except for about 1.5% of scattered pixels, the derived temperatures are between 10 K and 30 K. When there is no detection of the (2,2) line, we derive an upper limit to kinetic temperatures ( $T_k^u$ ) assuming  $3\sigma(2,2)$  intensity. Figure 2 shows the derived temperatures overlaid with the dust continuum and dust cores. The temperatures are generally lower toward the inside the dust cores, which has been demonstrated in paper I. A quantitative analysis of the thermal structure of the whole region is presented in Kauffmann et al. (2012).

The low velocity resolution of  $0.62 \text{ km/s}$  complicates the calculation of velocity dispersions. We first identify main group channels with signal-to-noise ratios  $> 3$  are identified. If more than one such channel is found, a dispersion  $\sigma_{\text{data}}$  is calculated, in which channels are weighted by their intensity; if a single channel is found, an upper dispersion limit of  $0.26 \text{ km/s}$  is adopted. The intrinsic dispersion of the (1,1) main group is then subtracted to obtain  $\sigma_{\text{obs}} = [\sigma_{\text{data}}^2 - (0.2 \text{ km/s})^2]^{1/2}$ . The value of the correction factor is derived from numerical simulations of lines with various optical depths. The pixel averaged velocity dispersion for dust cores are listed in Table 1.

## 4. DYNAMIC STATE OF CORES

For a full coverage of all OMC2 and OMC3 cores, we use the SCUBA survey of Orion by Nutter & Ward-Thompson (2007), who identified cores as ellipses in the signal to noise ratio map. We select SCUBA cores with

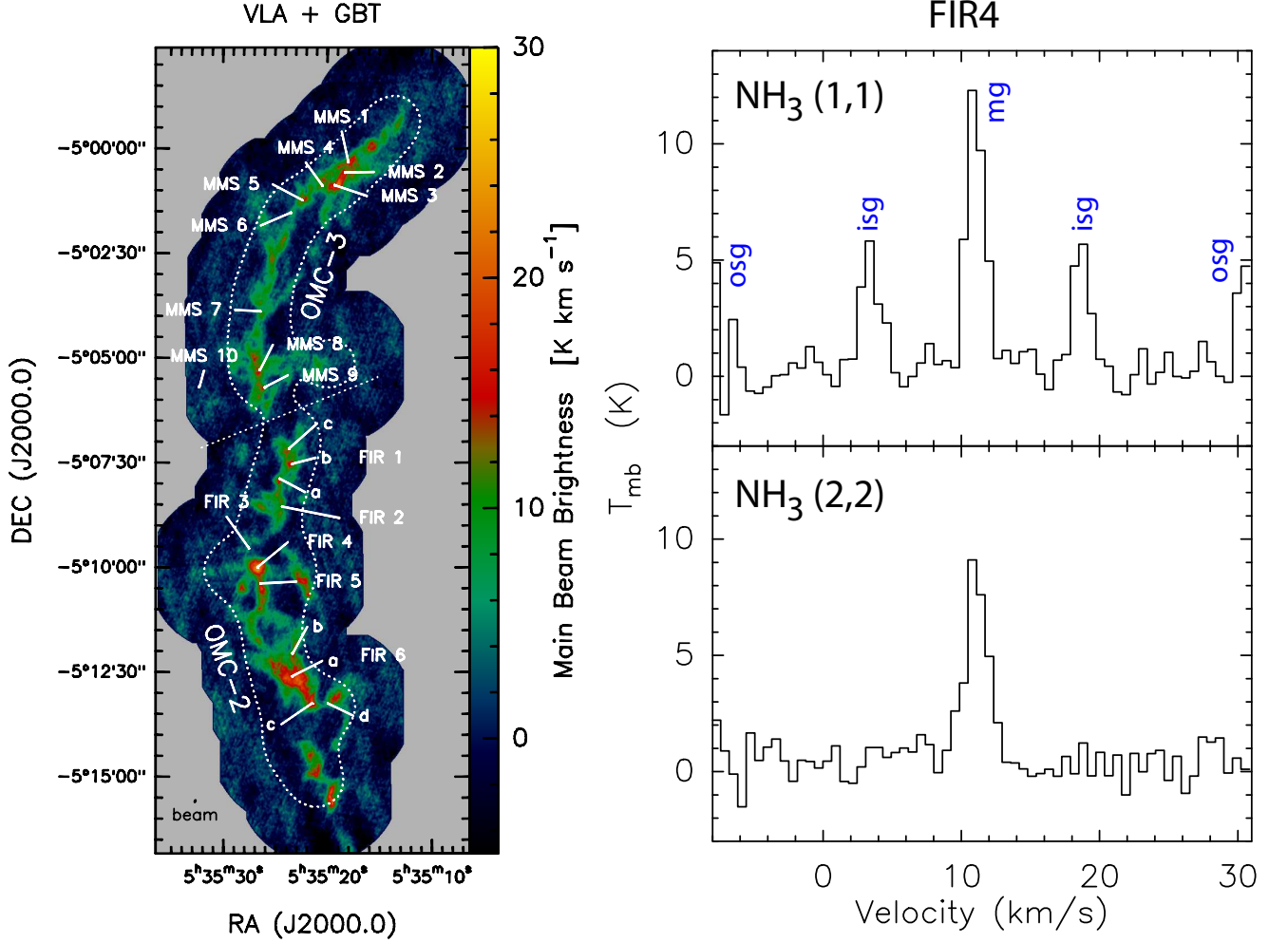


FIG. 1.— The integrated intensity of  $\text{NH}_3$  (1,1) overlaid with dust continuum peaks from Chini et al. (1997) and references therein. The white dotted line indicates the location where the gain drops to 80% of the peak value. The spectra shown on the right are for the FIR 4 position, the brightest  $\text{NH}_3$  peak in OMC 2. Due to the limitation of the VLA bandwidth, only the main group (mg) and the inner satellite groups (isg) of the hyperfine components are fully covered. The outer satellite groups (osg) are on the band edge.

more than 50% of the pixels having a measured  $T_k$  based on  $\text{NH}_3$ . These temperature measurements are weighted by dust column density and then averaged to be the core temperature  $T_{\text{core}}$ . Nutter & Ward-Thompson (2007) calculated dust mass assuming a uniform dust temperature of 20 K. In our map, 74% of the pixels have derived temperature lower than 20 K. We therefore scale the core mass by the factor  $B_{850,20\text{ K}}/B_{850,T_{\text{core}}}$ , where  $B_{850,T}$  is the Planck function at  $850\text{ }\mu\text{m}$  and temperature  $T$ . The resulting core mass is generally larger than what is reported in Nutter & Ward-Thompson (2007). The derived core temperatures and core velocity dispersion are reported in Table 1.

We identify cores with and without embedded stars based on Spitzer source identifications provided by T. Megeath. A core is deemed protostellar if the distance between its peak position and a YSO are less than the semi-minor axis of the core ellipse (Fig. 2 and Table 1).

#### 4.1. Are Cores Gravitationally Bound?

McKee & Zweibel (1992) derive the virial theorem in Eulerian form to express explicitly the contribution of turbulent pressure both inside and surrounding the cloud

$$2c_w(\mathcal{E} - \mathcal{E}_0) + \mathcal{M}_s + \mathcal{G} = 0, \quad (4)$$

where

$$c_w = 1 + \frac{\mathcal{E}_w - \mathcal{E}_{0w}}{2(\mathcal{E} - \mathcal{E}_0)} \quad (5)$$

is determined by the ratio of the difference between surface turbulent energy  $\mathcal{E}_{0w}$  and internal turbulent energy  $\mathcal{E}_w$ , and total surface kinetic energy  $\mathcal{E}_0$  and total internal kinetic energy  $\mathcal{E} = \frac{3}{2}M\sigma^2$ . For a cloud with primarily turbulent motions,  $c_w = 3/2$ . If steady motions, such as rotation, are significant,  $c_w$  is close to unity. The velocity resolution of our data limits our ability to probe the thermal linewidth. The existence of blending of hyperfine components in some spectroscopically resolved pixels (apparent  $\Delta V > 0.6\text{ km s}^{-1}$ ) suggests that the gas there is unlikely to be in a pure sonic state of either a  $\text{H}_2$  thermal linewidth of  $\Delta V \sim 0.3\text{ km s}^{-1}$  or even a  $\text{NH}_3$  thermal linewidth of  $\sim 0.08\text{ km s}^{-1}$ . For a large fraction of the pixels, however, we only have an upper limit to the linewidth. A unity  $c_w$  is assumed for simplicity for the virial mass calculation in this section.

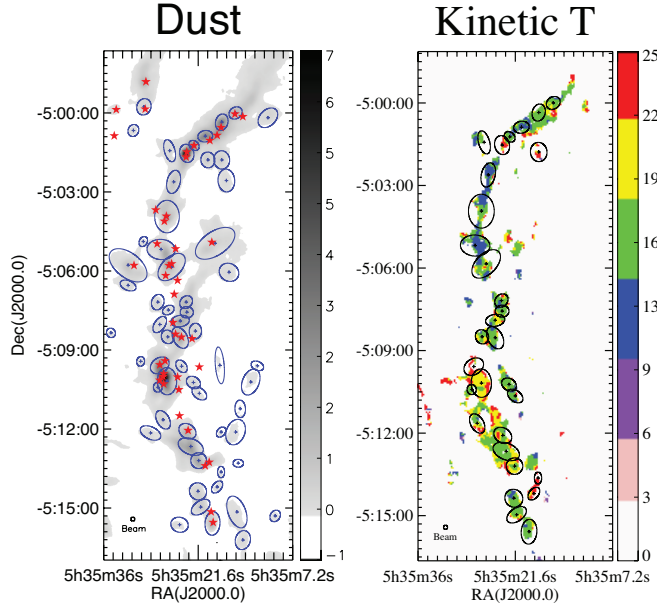


FIG. 2.— Left: 850  $\mu\text{m}$  dust images with fitted dust cores (Nutter & Ward-Thompson 2007). The red stars are embedded YSOs based Spitzer IRAC and MIPS surveys (T. Megeath, private communication). Right: Derived kinetic temperatures (no upper limits) overlaid with dust cores. Only cores with sufficient detection of temperature or upper limits (see discussion in the text) are plotted in this panel.

$\mathcal{M}_s$  is the magnetic energy associated with the cloud.  $\mathcal{G}$  is the gravitational potential energy. For an axisymmetric ellipsoid with concentric density profiles

$$\mathcal{G} = -\frac{3}{5}\alpha\beta\frac{GM^2}{r}, \quad (6)$$

where  $\beta = \arcsin e/e$  is the geometry factor determined by eccentricity  $e = \sqrt{1-f^2}$  and  $\alpha$  is determined by the density profile as being  $(1-a/3)/(1-2a/5)$  for a power law  $\rho \propto r^{-a}$  and 1.31 for an isothermal cloud in equilibrium (Bonnor 1956). The intrinsic axis ratio  $f$  is smaller than the observed axis ratio  $f_{obs}$  due to projection. Myers et al. (1991) show that dark cloud cores are more likely to be prolate. Condensations in Orion are also statistically more consistent with being prolate rather than oblate (Li 2002). Based on the more general inversion from Fall & Frenk (1983), we derive an averaged true axis ratio  $\bar{f}$  corresponding to a sample of a single value, namely, the observed  $f_{obs}$  for a prolate ellipsoid

$$\bar{f} = \frac{2}{\pi}f_{obs}\mathcal{F}_1(0.5, 0.5, -0.5, 1.5, 1, 1-f_{obs}^2), \quad (7)$$

where  $\mathcal{F}_1$  is the Appell hypergeometric function of the first kind. It is easy to verify that  $\bar{f} = 1$  for  $f_{obs} = 1$  and  $\bar{f} = 0$  for  $f_{obs} = 0$ . For values in between, we use the numerical value of  $\bar{f}$  as a replacement of  $f$  in calculating the gravitational potential.

By assuming  $\mathcal{M}_s = 0$  and  $\mathcal{E}_0 = 0$ , a simple virial mass can be derived using the virial theorem (Eq. 4)

$$M_{vir} = \frac{5}{\alpha\beta}\frac{\sigma^2 r}{G}. \quad (8)$$

The virial mass is the minimal mass for a cloud to be self-gravitating in the absence of pressure confinement and

steady magnetic field. A "virial mass ratio" independent of  $B$  and  $\mathcal{E}_0$  is defined as

$$R_{vir} = \frac{M}{M_{vir}}. \quad (9)$$

We find that 28 of 30 cores (Fig. 3 and Table 1), i.e., 93% have  $R_{vir} > 1$ , 15 cores (50%) fulfil  $R_{vir} > 5$ . The majority of the core sample are bound by gravity.

#### 4.2. Stability and Critical Mass

Now we consider the stability of cores with external pressure and the internal magnetic field. The critical mass  $M_C$  is defined as the maximum mass which can be stably supported by internal velocity dispersion and magnetic pressure. The two effects can be considered separately and then combined in a simple approximation

$$M_C = M_J + M_\Phi, \quad (10)$$

which is accurate to within 5% compared to the more rigorous calculations (McKee 1989).

The Jeans mass for a non-magnetic isothermal cloud (Bonnor 1956; McKee & Zweibel 1992) is

$$M_J = 1.182\frac{c_w^{3/2}}{c_{pr}^{1/2}}\frac{\sigma^4}{G^{3/2}P_{ic}^{1/2}}, \quad (11)$$

where  $c_w$  parametrizes the pressure from turbulence outside of the cloud and  $c_{pr}$  parametrize the added internal pressure from turbulence's disturbing B field. If we consider tracers of more diffuse gas in this region, such as  $^{13}\text{CO}$ , the linewidth is around  $1.5 \text{ km s}^{-1}$  (Melnick et al. 2011), definitely supersonic. We choose the combined factor to be in the middle of the possible range for turbulent gas  $c_w^{3/2}/c_{pr}^{1/2} \sim 2.1$  (McKee & Zweibel 1992).

The external pressure term can be estimated as

$$P_{ic} = n_{ic}\mu m_H \sigma_{ic}^2, \quad (12)$$

where the mean molecular weight  $\mu$  is 2.88 and  $m_H$  is the proton mass. We take a lower bound value of  $1 \text{ km s}^{-1}$  FWHM for estimating  $\sigma_{ic}$ . The inter-cloud density  $n_{ic}$  is not well known. Radiative transfer analysis of CO,  $^{13}\text{CO}$ , and  $\text{H}_2$  in this region (Li 2002) show that the densities are a few times  $10^4 \text{ cm}^{-3}$  in the relatively diffuse area. We use a lower bound of  $10^4 \text{ cm}^{-3}$  to calculate the Jeans mass given in Table 1. The Jeans mass thus derived will be a conservative upper limit.

The maximum mass which can be supported by a steady  $B$  field alone is

$$M_\Phi = c_\Phi \frac{\pi B r^2}{G^{1/2}}, \quad (13)$$

where  $c_\Phi \sim 0.12$  is given by numerical simulations (Mouschovias & Spitzer; Tomisaka, Ikeuchi & Nakamura 1988).

Crutcher et al. (1999) detect the Zeeman effect in the CN 3mm line near Orion BN/KL. The field strength is derived to be 0.19 mG or 0.36 mG, based on different fitting schemes. This is larger than the  $B \sim 0.03 \text{ mG}$  measured in dark clouds. Given the proximity of BN/KL to active star formation, the large  $B$  could be explained by rapid collapses' freezing magnetic flux into high density

regions along the line of sight. We thus take a smaller, nominal  $B = 0.1$  mG in our calculations of  $M_\Phi$ .

Using the critical mass calculated through Eq. 10, 11, and 13, we define the “critical mass ratio”

$$R_c = \frac{M}{M_c}. \quad (14)$$

We find that 26 out of 30 (87%) cores have  $R_c > 1$ , 22 cores (73%) fulfil  $R_c > 2$ . The majority of the Orion massive cores are supercritical.

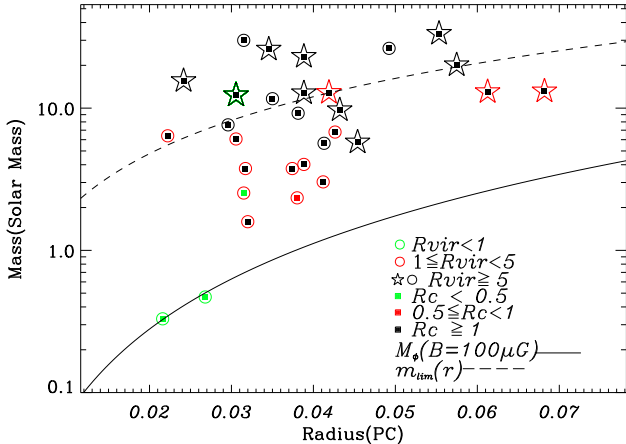


FIG. 3.— The mass and size of cores plotted in the same fashion as in paper II. The colors of the the open symbols denote the virial mass ratio  $R_{vir}$ , with green for a value smaller than 1, red for between 1 and 5 and black for  $> 5$ . Open stellar symbols are for cores containing a protostar and open circles are for starless cores. The colors of the solid squares denote the critical mass ratio, with green for  $< 1$  and black for  $> 1$ . The solid curve is for mass supported a steady magnetic field of  $100 \mu\text{G}$ . The dashed curve is for the empirical threshold for massive star formation (Eq. 15).

#### 4.3. Discussion: Is Orion Special?

Our data suggest mass ratios  $R_{vir} > 5$  and  $R_c > 1$  for most cores. This is different from other clouds in solar neighborhood within  $\sim 500$  pc. In Perseus, for example, Foster et al. (2008) and Kirk et al. (2007) find an equivalent  $R_{vir} \lesssim 3$ . For Ophiuchus, the observations of André et al. (2007) imply  $R_{vir} \leq 1$  based on their Table 4 after adopting the dust opacity used here. For SCUBAidentified Gould Belt cores, Sadavoy et al. (2010) find that only 20 cores out of a total of 354 have  $M/M_J \gtrsim 2$  (using our dust opacities, and excluding their Orion data to reduce sample overlap).” Their  $M_J$  represents a purely thermal Jeans mass, which means that these cores will have an even smaller mass ratio using definitions in this paper.

The observed  $R_{vir}$  in Orion may be similar to those found in high mass star forming regions, e.g., the two

clouds studied by Pillai et al. (2011). Although direct comparison is hard due to the much larger distance of other high star forming regions.

The calculations differ slightly between studies, e.g., in the factors  $\alpha$ ,  $\beta$ , and dust opacities. These differences alone cannot explain the larger mass ratios observed in Orion. Thus, our result that 50% of Orion cores have  $R_{vir} > 5$  and 73% are supercritical is significant.

The  $\text{NH}_3$  lines are not well resolved in our data with a channel width of  $0.62 \text{ km s}^{-1}$ . Using the channel width as the upper limit of the intrinsic line width, the velocity dispersion of Orion cores cannot significantly exceed those of the cores in other regions studied by Kirk et al. (2007), André et al. (2007), and Foster et al. (2008). The high mass ratios is thus a result of higher masses for Orion cores.

Kauffmann et al. (2010) propose an empirical threshold for massive star formation

$$m_{\text{lim}}(r) = 870 M_\odot (r/\text{pc})^{1.33}. \quad (15)$$

We indeed find 12 cores (40%) above this threshold. The excess is not dramatic, but consistent with Orion cores being different from other nearby star forming regions in them being more massive and more likely to form massive stars.

#### 5. CONCLUSIONS

We have mapped OMC2 and OMC3 in  $\text{NH}_3$  (1,1) and (2,2) with both VLA and GBT. The combined single dish plus interferometric data provide a rare detailed look into the thermal and dynamic properties of a collection of massive quiescent cores. Our main results are:

1. We obtain good temperature measurement for 30 dust cores. The median core temperature is 17 K. The typical uncertainty for derived temperature of each pixel is about 2 K.
2. 12 cores are associated with a protostar. The average temperatures of the protostellar and the starless cores are similar suggesting that the heating in OMC2-3 region is primarily external.
3. A total of 28 cores (93%) are gravitationally bound ( $R_{vir} > 1$ ), and 15 cores (50%) achieve  $R_{vir} > 5$ . Compared to other Gould Belt clouds, a much higher fraction of cores are tightly bounded.
4. 26 out of 30 cores (87%) are more massive than the critical mass defined as the combination of Jeans mass and mass supported by a steady magnetic field of  $100 \mu\text{G}$ .

In summary, this sample of Orion cores, identified in dust emission with temperature and turbulence measured in  $\text{NH}_3$  inversion lines, are proven to be well bounded by gravity and are mostly supercritical. They will evolve rapidly, either collapsing to form a star or fragmenting.

#### REFERENCES

- André, P., Belloche, A., Motte, F., & Peretto, N. 2007, *A&A*, 472, 519  
 Benson, P. J. & Myers, P. C. 1989, *ApJS*, 71, 89  
 Bonnor, W. B. 1956, *MNRAS*, 116, 351  
 Chini, R., Reipurth, B., Ward-Thompson, D., et al. 1997, *ApJ*, 474, L135  
 Crutcher, R. M., Troland, T. H., Lazareff, B., Paubert, G., & Kazès, I. 1999, *ApJ*, 514, L121

TABLE 1  
TEMPERATURES AND ENGERGY STATE OF ORION CORES

Source	RA (J2000)	DEC (J2000)	$T_{core}$ K	$\sigma_{core}$ km s <sup>-1</sup>	Mass M <sub>☉</sub>	$R_{vir}$	$R_c$	YSO RA (J2000)	YSO DEC (J2000)	Seperation <sup>a</sup> Arcsec
OrionAN-535161-50000	0:20:00	-5:00:00	16.	0.26	12.	17.	9.	5:35:16	-5:00:02	2.7
OrionAN-535182-50021	0:20:00	-5:00:00	16.	0.36	26.	11.	4.	5:35:18	-5:00:33	12.1
OrionAN-535182-50147	0:20:00	-5:00:00	21.	0.27	3.	3.	1.	5:35:20	-5:01:02	51.9
OrionAN-535183-51338	0:20:00	-5:00:00	31.	0.26	0.3	0.7	0.3	5:35:20	-5:13:15	35.1
OrionAN-535189-51412	0:20:00	-5:00:00	30.	0.27	0.5	0.8	0.4	5:35:20	-5:13:23	55.4
OrionAN-535196-51535	0:20:00	-5:00:00	15.	0.26	6.	6.	3.	5:35:19	-5:15:32	2.7
OrionAN-535207-50053	0:20:00	-5:00:00	14.	0.26	30.	41.	22.	5:35:20	-5:01:02	14.2
OrionAN-535214-51458	0:20:00	-5:00:00	19.	0.27	4.	4.	2.	5:35:19	-5:15:08	26.1
OrionAN-535216-51039	0:20:00	-5:00:00	16.	0.26	2.	2.	1.	5:35:24	-5:10:30	47.1
OrionAN-535217-51312	0:20:00	-5:00:00	24.	0.26	9.	9.	5.	5:35:20	-5:13:23	18.9
OrionAN-535218-51422	0:20:00	-5:00:00	16.	0.26	6.	5.	3.	5:35:19	-5:15:08	55.3
OrionAN-535224-50114	0:20:00	-5:00:00	19.	0.26	16.	28.	15.	5:35:22	-5:01:14	0.1
OrionAN-535225-51014	0:20:00	-5:00:00	15.	0.35	2.	1.	0.4	5:35:24	-5:10:30	36.6
OrionAN-535229-51240	0:20:00	-5:00:00	17.	0.31	26.	13.	6.	5:35:23	-5:12:03	37.4
OrionAN-535234-51205	0:20:00	-5:00:00	17.	0.27	13.	13.	7.	5:35:23	-5:12:03	2.4
OrionAN-535235-50132	0:20:00	-5:00:00	27.	0.32	23.	12.	6.	5:35:23	-5:01:28	3.3
OrionAN-535235-50734	0:20:00	-5:00:00	16.	0.26	8.	11.	6.	5:35:25	-5:07:57	39.1
OrionAN-535236-50711	0:20:00	-5:00:00	17.	0.32	6.	4.	2.	5:35:25	-5:06:52	32.4
OrionAN-535245-50754	0:20:00	-5:00:00	15.	0.26	12.	16.	8.	5:35:25	-5:07:57	16.8
OrionAN-535245-50832	0:20:00	-5:00:00	18.	0.31	10.	6.	3.	5:35:24	-5:08:30	3.3
OrionAN-535255-50237	0:20:00	-5:00:00	15.	0.31	7.	4.	2.	5:35:23	-5:01:40	63.4
OrionAN-535258-50551	0:20:00	-5:00:00	19.	0.31	13.	5.	2.	5:35:26	-5:05:47	7.0
OrionAN-535261-50126	0:20:00	-5:00:00	16.	0.30	4.	3.	1.	5:35:23	-5:01:28	38.9
OrionAN-535264-50830	0:20:00	-5:00:00	18.	0.26	4.	5.	3.	5:35:25	-5:08:23	18.9
OrionAN-535265-50356	0:20:00	-5:00:00	19.	0.32	13.	4.	2.	5:35:26	-5:03:55	1.7
OrionAN-535265-51011	0:20:00	-5:00:00	23.	0.31	34.	14.	8.	5:35:27	-5:10:17	9.7
OrionAN-535271-51139	0:20:00	-5:00:00	20.	0.31	2.	2.	0.7	5:35:24	-5:11:29	38.5
OrionAN-535274-50511	0:20:00	-5:00:00	13.	0.28	20.	11.	6.	5:35:28	-5:04:58	15.7
OrionAN-535276-50935	0:20:00	-5:00:00	28.	0.35	13.	5.	2.	5:35:27	-5:09:33	1.5
OrionAN-535279-51025	0:20:00	-5:00:00	17.	0.34	6.	5.	1.	5:35:27	-5:10:17	15.5

<sup>a</sup> The angular distance between dust continuum peaks and their respective closest YSOs.

Foster, J. B., Rosolowsky, E. W., Kauffmann, J., et al. 2009, ApJ, 696, 298  
Ho, P. T. P. & Townes, C. H. 1983, ARA&A, 21, 239  
Ikeda, N., Sunada, K., & Kitamura, Y. 2007, ApJ, 665, 1194  
Kauffmann et al. 2012, in prep.  
Kirk, H., Johnstone, D., & Tafalla, M. 2007, ApJ, 668, 1042  
Könyves, V., André, P., Men'shchikov, A., et al. 2010, A&A, 518, L106  
Li, D. 2002, Ph.D. Thesis,  
Li, D., Goldsmith, P. F., & Menten, K. 2003, ApJ, 587, 262 (Paper I)  
Li, D., Velusamy, T., Goldsmith, P. F., & Langer, W. D. 2007, ApJ, 655, 351 (Paper II)  
McKee, C. F. 1989, ApJ, 345, 782  
McKee, C. F. & Zweibel, E. G. 1992, ApJ, 399, 551  
Mookerjee, B., Kramer, C., Nielbock, M., & Nyman, L.-Å. 2004, A&A, 426, 119  
Mouschovias, T. C. & Spitzer, L. 1976, ApJ, 210, 326  
Myers, P. C., Fuller, G. A., Goodman, A. A., & Benson, P. J. 1991, ApJ, 376, 561  
Pillai, T., Kauffmann, J., Wyrowski, F., et al. 2011, A&A, 530, A118

Reid, M. A., & Wilson, C. D. 2005, ApJ, 625, 891  
Sadavoy, S. I., Di Francesco, J., Bontemps, S., et al. 2010, ApJ, 710, 1247  
Takahashi, S., Saito, M., Ohashi, N., et al. 2008, ApJ, 688, 344  
Tatematsu, K., Kandori, R., Umemoto, T., & Sekimoto, Y. 2008, PASJ, 60, 407  
Tomisaka, K., Ikeuchi, S., & Nakamura, T. 1988, ApJ, 335, 239  
Velusamy, T., Peng, R., Li, D., Goldsmith, P. F., & Langer, W. D. 2008, ApJ, 688, L87 (Paper III)  
Vogel, S. N., Wright, M. C. H., Plambeck, R. L., & Welch, W. J. 1984, ApJ, 283, 655  
Ward-Thompson, D., André, P., Crutcher, R., Johnstone, D., Onishi, T. & Wilson, C. 2007, Protostars and Planets V, 33  
Williams, J. P., Plambeck, R. L., & Heyer, M. H. 2003, ApJ, 591, 1025  
Wiseman, J. J. & Ho, P. T. P. 1998, ApJ, 502, 676  
Zhang, Q., Ho, P. T. P., & Wright, M. C. H. 2000, AJ, 119, 1345